

Large exciton binding energies in MnPS_3 as a case study of vdW layered magnet

Magdalena Birowska*

University of Warsaw, Faculty of Physics, 00-092 Warsaw, Pasteura 5, Poland

Paulo E. Faria Junior[†] and Jaroslav Fabian[‡]

Institute for Theoretical Physics, University of Regensburg, 93040 Regensburg, Germany

Jens Kunstmann[§]

Department of Chemistry and Food Chemistry TU Dresden, 01062 Dresden, Germany

(Dated: February 19, 2021)

Stable excitons in semiconductor monolayers such as transition-metal dichalcogenides (TMDCs) enable and motivate fundamental research as well as the development of room-temperature optoelectronics applications. The newly discovered layered magnetic materials present a unique opportunity to integrate optical functionalities with magnetism. We predict that a large class of antiferromagnetic semiconducting monolayers of the MPX_3 family exhibit giant excitonic binding energies, making them suitable platforms for magneto-optical investigations and optospintronic applications. Indeed, our investigations, based on first principles methods combined with an effective-model Bethe-Salpeter solver, show that excitons in bare Neel- MnPS_3 are bound by more than 1 eV, which is twice the excitonic energies in TMDCs. In addition, the antiferromagnetic ordering of monolayer samples can be inferred indirectly using different polarization of light.

The research on the atomically thin materials has emerged to be one of the most active topics since the discovery of graphene. The family of two-dimensional (2D) materials has grown rapidly and now comprises a broad class of structures including metals, semimetals, semiconductors, insulators, and topological insulators. Only recently, in 2017, magnetic materials have been added to the family of 2D crystals, when the intrinsic ferromagnetism was experimentally reported for CrI_3 [1] and $\text{Cr}_2\text{Ge}_2\text{Te}_6$ [2]. This breakthrough triggered the interest in searching for other 2D materials with intrinsic magnetic ordering [3–6]. These 2D magnetic materials are important for fundamental physics, as well as for technological applications in non-volatile information storage, spin injection, filtering, and detection on atomically thin scale.

One source of 2D magnetic materials are layered magnets [5], consisting of vertically stacked layers, weakly bonded via van der Waals forces. These weak forces enable the low cost fabrication of 2D magnets by using the mechanical exfoliation technique instead of the more sophisticated molecular beam epitaxy method. Furthermore, combining two different types of 2D materials in one heterostructure can result in new phenomena or new features, not present in the individual layers [7–11]. Similarly, combining various 2D magnets in vdW heterostructures may result in exotic spin textures and new properties not exhibited in adjacent layers leading to new types of spintronic devices.

Metal phosphorus trichalcogenides (MPX_3 , with $\text{M} =$

$\text{V, Cr, Mn, Fe, Co, Ni}$ etc. and $\text{X} = \text{S, Se, Te}$) are vdW magnets which were widely studied in the bulk form already in the 80s and 90s of the last century [12, 13]. Ultrathin layers have been obtained by using chemical vapor deposition and exfoliation methods and are the subject of the research of recent years (see the review [14]). This class of materials exhibit intrinsic antiferromagnetism (AFM) with diverse magnetic configurations of the transition metal ions [15], such as MnPS_3 with the Neel Temperature of 78 K [16]. The research on MPX_3 is not only crucial from the point of view of fundamental studies [17], but as recent reports show these materials can be a platform for field effect transistors [18, 19], photodetectors [20, 21], or tunneling devices [22]. Important for experimental investigations, monolayers are relatively stable in air [18, 23, 24].

In this study, we systematically investigate various magnetic states of bulk and monolayer MnPS_3 as the representative material of magnetic vdW layered MPX_3 systems. Starting from first-principles calculations based on the DFT+U scheme, we identify the position in k -space of the conduction (valence) band minima (maxima) and their (anisotropic) effective masses. Furthermore, we determine material specific static dielectric constants and polarizabilities, the building blocks for the screened electron-hole interaction. The impact of the U parameter is also investigated, showing moderate influence on the optical properties. Finally, using the calculated DFT quantities combined with the versatile formalism of the effective BSE, we explore the exciton binding energies. Our calculations reveal that excitons in bare monolayer Neel- MnPS_3 are bound by more than 1 eV, exceeding the values in TMDCs, advancing air stable MPX_3 as an exciting new playground for studying optical and magnetic properties, and their interplay.

DFT+U calculations.—We consider the impact of the

* Magdalena.Birowska@fuw.edu.pl

[†] fariajunior.pe@gmail.com

[‡] jaroslav.fabian@ur.de

[§] jens.kunstmann@chemie.tu-dresden.de

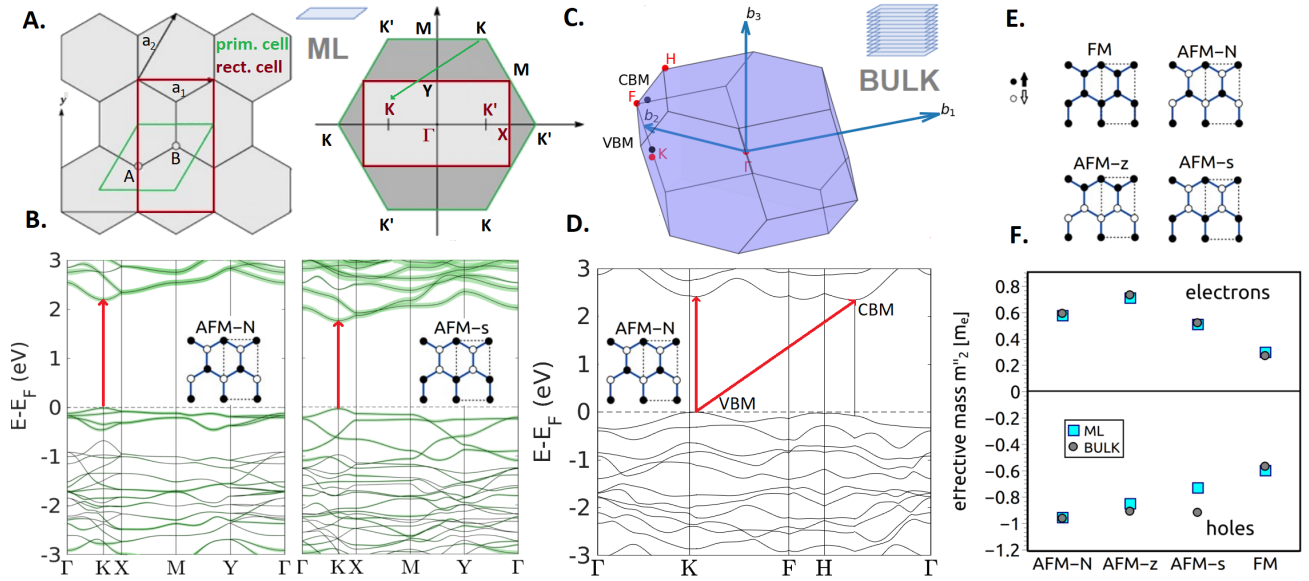


FIG. 1. Electronic structure of MnPS_3 systems. (A) Primitive (green) and extended (red) unit cells for monolayers (ML) and their corresponding first Brillouin zones (BZ) and their special points. (B) Band structures of the magnetic states AFM-N and AFM-s ($U=3\text{eV}$) with projections of Mn 3d orbitals (spin up) superimposed in green. The rectangular supercell has been used to facilitate comparison. (c) BZ for bulk corresponding to the primitive unit cell with special points indicated in red. (D) Bulk band structure for the AFM-N magnetic ground state ($U=5\text{eV}$). VBM and CBM are located at non-special k-points which are also indicated as a black circles in (C). The red arrows indicate the band gaps. The difference between the indirect (ID, slanted arrow) and direct (D, straight arrow) band gaps is just a few tens of meV (for the exact values see SM). (E) Spin arrangement of the Mn atoms in the considered magnetic states. (F) In-plane components of the effective mass tensor of electrons and holes for $U=5\text{eV}$.

various magnetic states, such as the AFM-Neel (AFM-N) which is a groundstate [25–27], and other metastable states, i. e., AFM zigzag (AFM-z), AFM-stripy (AFM-s) and ferromagnetic state (FM) on the character of the band gap, the band alignments, and the position of the band extrema, namely valence band maximum (VBM) and conduction band minimum (CBM). In order to account for these various magnetic states of MnPS_3 , the laterally rectangular supercell was chosen (see Fig. 1 (A)). Generally, our results demonstrate that the monolayers with various magnetic orderings exhibit a direct band gap at the high-symmetry point K of the first Brillouin zone (BZ), consistent with previously reported results for the ground state configuration [26] (see Fig. 1 (B)).

The differences in the band alignments, band crossing or the curvature of the bands near the VBM and CBM between the AFM-N and AFM-s magnetic configurations are clearly visible (see Fig. 1 (B)). Note that both the VBM and the CBM regions are composed of 3d states coming from the Mn ions. In addition, the position of the VBM and the CBM for the monolayer is affected neither by the U parameter, nor by the magnetic state (for details see Supplemental Material (SM)), where the comparison with hybrid functional HSE06 is presented). We emphasize that the DFT+U approach provides quantitatively predictive results for many correlated systems (see review [28]).

Let us now focus on the bulk MnPS_3 calculations. The

electronic band structure for the magnetic ground state (AFM-N) is presented in Fig. 1(D) along high-symmetry points, with the position of the VBM and CBM indicated by the black circles in 1(C).

The indirect band gaps are obtained for all magnetic states and for both U values (see Table S5). We want to emphasise, that we precisely probe the first BZ to directly state the position of the band edges. We found that the band extrema are located in non-special k-points (see SM). However, the bands close to the Fermi level are very flat (see points H and K have close energies to VBM, see Fig. 1 (D)). Therefore, the difference between the indirect and direct band gaps are very small, e.g. for AFM-N it is just 17 meV for $U=5\text{eV}$ (indirect 2.352 eV vs. direct 2.369 eV). The direct transition occurs near to the “K” point (Fig. 1 (D)) and is in perfect agreement with previously reported results equal to 2.37 eV (at K, with approach PBE+D2+U=5eV) [27]. Due to the fact that the differences between the direct and indirect transitions are small, we introduce the term quasi-direct band gap systems for such cases. The exact coordinates of high symmetry k-points, the positions of VBM and CBM are collected in Table S5. Our calculations reveal that the position of the bands extrema are generally independent of the U parameter used.

By properly identifying the band extrema, we can then extract the effective mass tensor for monolayer and bulk structures, for all magnetic orderings considered (see

Fig. 1 (F)). We found that the effective masses depend strongly on the magnetic configuration. Namely, the smaller values are obtained for FM state than the masses obtained in the case of AFM configurations. For the AFM arrangements, the differences from a few tenths to a few hundredths of the rest electron mass are visible. In addition, the effective mass of holes is approximately two times heavier than the effective mass of electrons (the exact values for monolayer and bulk are given in Table S4 and Table S5, respectively). Note that the differences between the effective masses of bulk and monolayers are negligible (see Fig. 1 (F), where the effective mass along [010], m_2^{\parallel} , is compared), revealing that the mutual layered interactions of vdW-type do not alter the curvature of the valence and conduction band edges. In the case of the monolayer systems, the obtained principle reciprocal axes coincide with the Cartesian reciprocal axes, whereas in the case of the bulk systems only m_2^{\parallel} is parallel to [010] crystallographic direction, the other two are shifted (see SM). In addition, the effective masses depend on the Hubbard U parameter. Generally, the smaller effective masses are obtained for U=5eV in comparison to U=3eV, which has an origin in the position of the d -states, i. e., the U values push the d -states away from the Fermi level (see SM). In addition, the anisotropic behaviour of the in-plane components are observed especially for AFM-s and AFM-z for monolayer as well as for the bulk systems (for the details see SM). The calculated values of the effective masses also provide important information for the transport experiments[22].

We now describe dielectric properties of the studied systems by means of density functional perturbation theory in the independent particle (IP) approach neglecting local field effects [29]. Although this approach is known to slightly overestimate the dielectric constants of semiconducting bulk crystals by up to 20 % [29], post-DFT schemes such as single-shot G_0W_0 approximation are still restricted to few-atoms systems and require thousands of the conduction bands to reach convergence [30, 31]. Note that even fully self-consistent GW approaches [31–33] overestimates the bulk band gaps, which is likely due to underestimation of the macroscopic dielectric constant. In addition, the overestimation of the dielectric constant in the IP approach indicates that the exciton binding energy might be even larger than what is obtained in this study (in 2D systems the the exciton binding energy is inversely proportional the dielectric screening). Therefore, the IP approach is a reasonable choice for the system size considered here (up to 20 atoms in the supercell).

Our results demonstrate that the in-plane components of static dielectric constants are isotropic for both monolayer and bulk systems. Generally, the static dielectric constants are independent of the magnetic ordering and there is only a slight dependence on the value of the Hubbard U parameter (up to 5% difference between the U=5eV and U=3eV). Note that the layered MnPS₃ material has substantially weaker screening ($\epsilon^{\parallel} = 7.75$ and $\epsilon^{\perp} = 5.88$ for U=3eV, see the Table S2) than MoS₂

layered system with components of dielectric constants equal to $\epsilon^{\parallel} = 15.4$ and $\epsilon^{\perp} = 7.43$ [34]. In addition, the out-of-plane components are lower than the corresponding in-plane ones for the bulk system, a typical feature also in other layered materials.

It is crucial to mention that the dielectric tensor is well defined for the bulk materials. In order to compare the results obtained for the bulk and monolayer systems, we calculate the 2D polarizability χ_{\parallel} (for the details see SM). Our results reveal that the polarizability does not depend on the magnetic ordering and is about 3.5 Å for U=3 eV (3.3 Å for U=5eV). This value is approximately two times lower than obtained for other layered materials such as MoS₂ (6.60 Å), WSe₂ (7.18 Å) or MoSe₂ (8.23 Å) [35]. In addition, our results reveal negligible impact of magnetic state and the Hubbard U parameter on the dielectric properties of MnPS₃ systems, thus indicating that the screening is mainly performed by s , p orbitals (U parameter affects the d states). This is in line with the common knowledge concerning the d orbitals, which exhibit weak screening behaviour. We have so far discussed only the electronic contribution to the dielectric screening. Since the bonding in MnPS₃ is partially ionic, phononic contributions are important for the total value of the static dielectric constant (see SM). However, these contributions do not seem to effectively impact the screening of the electron-hole interactions[36], mainly because they operate at different energy scales. We note here that the deep analysis of the phononic contribution is out of the scope of the present paper and will be studied elsewhere.

Excitonic properties.—An exciton is the bound state formed by an electron and a hole, thus, an intrinsic many-body phenomena. One possibility to account for the electron-hole interaction is to employ the Bethe-Salpeter equation (BSE) [37, 38]. Although capable of describing realistic optical spectra, the full implementation of the BSE within first principles (using DFT energies and wavefunctions, for instance) requires a high computational cost. However, it is possible to bypass these difficulties by considering effective models, parametrized by *ab initio* calculations. For instance, it has been recently shown that using the BSE approach with effective models for the band structure and for the screened electron-hole interactions, it is possible to obtain reliable results for excitons in monolayers (TMDCs and phosphorene, for example) [39–44] and proximitized TMDCs in vdW heterostructures[10, 45–47]. Particularly in the context of 2D magnetic systems, the successful combination of DFT+U calculations and the effective BSE formalism in TMDC/CrI₃ systems by Zollner et al.[10] provided reliable estimations to the the valley Zeeman proximity exchange signatures in the optical spectra of WSe₂/CrI₃[48, 49] and, more interestingly, to the linear dependence with respect to out-of-plane electric fields in MoSe₂/CrBr₃[50].

To investigate the band-edge excitons in bulk and monolayer MnPS₃ we then use the versatile formalism

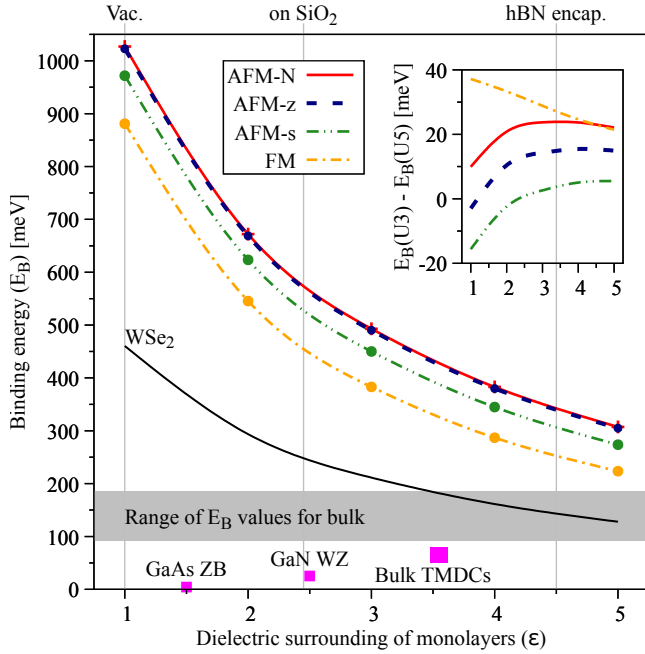


FIG. 2. Large exciton binding energies E_B (below the band gap), for the different AFM and FM phases in monolayer and bulk MnPS_3 . For the monolayer we show the evolution of E_B as a function of the dielectric screening of the surroundings. The values for air/vacuum, SiO_2 [39] substrate and hBN encapsulation [51] are indicated by vertical lines. The inset on the top right corner shows the difference of E_B for $U=3\text{eV}$ and $U=5\text{eV}$. As a representative example of TMDC monolayers, we show E_B for WSe_2 (taken from Ref. 42). The range of calculated values of E_B for bulk MnPS_3 is shown by the shaded region. Values for typical bulk compounds are also shown for comparison: $E_B = 4.2$ meV for GaAs zinc-blende [52], $E_B = 25.2$ meV for GaN wurtzite [53] and for bulk TMDCs ranging from 50 to 80 meV [54–57]. For the bulk E_B , the x-axis is meaningless.

of the BSE with effective models [38, 43, 58], which allows for exciton calculations with general band structure dispersion and electrostatic potentials, either for direct or indirect excitons. Particularly, we treated the conduction and valence bands with anisotropic quadratic dispersion, i.e., different effective masses along the different axes (see SM). The electron-hole interaction for monolayers is mediated by the Rytova-Keldysh potential [59, 60], which requires the screening length of the 2D material and the effective dielectric constant, ϵ , of the surroundings to simulate effects of the substrate and/or encapsulation. For the bulk case, electrons and holes interact via the anisotropic Coulomb potential [61] which requires the static dielectric constant along the different directions of the crystal. Therefore, in summary, in the effective BSE description the excitonic properties are determined by two parameters: the effective masses in conduction and valence bands, and the static dielectric function (in bulk) or the screening length (in monolayer). These properties are discussed in the DFT+U section. For the explicit

form of the BSE, band dispersion, electron-hole potentials, parameters and computational details, see Sec. I B. in the SM.

In Fig. 2 we summarize our findings for the exciton binding energies (E_B). Our calculations revealed that E_B in bare ($\epsilon = 1$) monolayer MnPS_3 is quite large, reaching values slightly above 1 eV for the AFM-N phase. The other phases also show sizeable values: the E_B of AFM-z has nearly the same value as the E_B of AFM-N while the E_B of AFM-s (FM) phase is approximately 50 (150) meV smaller than the E_B AFM-N phase. These energy differences between the different phases remain quite similar in the range of effective dielectric constant of the environment. Furthermore, changing U from 3 eV to 5 eV preserves the same energetic ordering of E_B for the different phases (the effect of U on the E_B is around tens of meV, shown in the inset of Fig. 2). These values are around twice the values of the binding energies in conventional TMDCs (such as WSe_2 , as shown in Fig. 2). The values of E_B for the bulk case are also shown in Fig. 2 to compare with the values of the monolayers, even though the x-axis (dielectric constant of the surroundings) has no meaning. We found E_B in the range of 90 to 180 meV considering the different phases and values of $U=3\text{eV}$ and $U=5\text{eV}$. All the calculated values for E_B in the monolayer and bulk cases are given in the SM.

TABLE I. Calculated optical selection rules from VBM to CBM for the different AFM magnetization of the monolayer systems, highlighting the polarization and intensity. The intensity is given by $\left| \frac{\hbar}{m_e} \hat{e} \cdot \vec{p}_{cv} \right|^2$ in which $\hat{e} = \{\hat{x}, \hat{y}, \hat{z}\}$ is the light polarization and \vec{p}_{cv} is the matrix element between CBM and VBM.

	Magnetization	U [eV]	Polarization	Intensity $[(\text{eV}\text{\AA})^2]$
AFM-N	3	z	0.303	
	5	z	0.281	
AFM-z	3	y	0.159	
	5	y	0.082	
AFM-s	3	y	0.034	
	5	y	0.025	

For monolayer systems the selection rules have been determined (see Table I) for the direct transitions between VBM and CBM, following Ref. [62]. We found that the dipole matrix elements exhibit different non-zero components for the different magnetic states. Namely, the AFM-N case shows out-of-plane component (along z), whereas for AFM-z and AFM-s only the in-plane component (along y) is non-zero, with different intensities for each case. For the FM case, no optical transitions are allowed. Combined with the calculated exciton binding energies, the selection rules provide additional support that the different magnetic configurations can be distinguished optically.

Conclusions.— All magnetic states of monolayers employed in this study exhibit a direct band gap at the high-symmetry K points. For the bulk systems, the band gap is quasi-direct located at non-special k-points and with a moderate impact of the magnetic state on the position of the VBM and CBM. We found a strong impact of the magnetic state on the electron and hole effective masses, with moderate influence from value of the Hubbard U parameter. Generally, the in-plane components of the effective mass tensor of bulk systems and metastable anti-ferromagnetic cases of the monolayers are anisotropic. Based on the DFT+U results, we calculated the dielectric constants and 2D polarizabilities, the building blocks to model screened electron-hole interactions. The key result of our study is that the exciton binding energies are large in comparison to many other layered semiconductors such as TMDs, for both monolayer and bulk systems. In particular, we found exciton binding energies of about 1 eV for the bare monolayer, which are about two times larger than the typical values in TMDCs. In addition, the exciton binding energies in bulk systems are about one order of magnitude larger than the ones of conventional bulk semiconductors. Analyzing the effect of the Hubbard U parameter, we found that the exciton binding energies vary on a scale of tens of meV for U=3eV to 5eV. Our results suggest that the magnetic state might be inferred indirectly from the absorption onset in optical measurements, and, particularly, that the antiferromagnetic configuration of monolayer systems is sensitive to the polarization of the light.

M.B. acknowledges financial support from the National Science Centre, Poland on the basis of the decision no. DEC-2016/23/D/ST3/03446, within the framework of the research project ‘SONATA 12’ no. UMO-2016/23/D/ST3/03446. Financial support from the Deutsche Forschungsgemeinschaft (DFG, German Research Foundation) under Project-ID 314695032 (SFB 1277) is acknowledged by P.E.F.J. and J.F. and under Project-ID 317551441 by J.K. Access to computing facilities of TU Dresden (ZIH) within the project “TransPheMat”, PL-Grid Polish Infrastructure for Supporting Computational Science in the European Research Space, and of the Interdisciplinary Center of Modeling (ICM), University of Warsaw are gratefully acknowledged.

Supplementary Material: Large exciton binding energies in MnPS₃ as a case study of vdW layered magnet

Magdalena Birowska,^{1,*} Paulo E. Faria Junior,²
Jaroslav Fabian,² and Jens Kunstmann³

¹University of Warsaw, Faculty of Physics,
00-092 Warsaw, Pasteura 5, Poland

²Institute for Theoretical Physics, University of
Regensburg, 93040 Regensburg, Germany

³Department of Chemistry and Food Chemistry TU
Dresden, 01062 Dresden, Germany

*Electronic address: Magdalena.Birowska@fuw.edu.pl
(Dated: February 19, 2021)

CONTENTS

I. Computational Details	1
A. DFT calculations	1
Effective masses	2
Dielectric screening	2
Selection rules	3
B. Exciton calculations	3
II. Results	4
A. DFT studies.	4
B. Exciton binding energies	5
References	5

I. COMPUTATIONAL DETAILS

A. DFT calculations

The bulk MnPS₃ compound exhibits the monoclinic space group symmetry *C2/m*. We have chosen the smallest possible supercell which reflects the particular magnetic configuration. Namely, AFM-N and FM arrangements can be represented in primitive unit cell (10 atoms in the supercell, denoted in Table S1 as “p”), whereas the AFM-z and AFM-s extended (laterally rectangular supercell is used, consists of 20 atoms, denoted in Table S1 as “e”). The basis vectors and corresponding reciprocal lattice vectors are collected in Table S1.

The calculations are performed in the framework of spin-polarised density functional theory (DFT) as implemented in VASP package [63, 64]. The Perdew–Burke–Ernzerhof (PBE) exchange–correlation functional is employed. The electron-ion interaction is modeled using projector augmented wave (PAW) pseudopotentials. The kinetic energy cutoff for the plane-wave expansion of the pseudo-wave function is set to 400 eV. A k-mesh of 10×10×2 for ML “p”, 10×6×2 for ML “e” (10×10×9 for bulk “p”, 10×6×9 for bulk “e”)

TABLE S1. The BZ is spanned by three reciprocal lattice vectors \vec{b}_1 , \vec{b}_2 and \vec{b}_3 constructed from the basis vectors \vec{a}_1 , \vec{a}_2 and \vec{a}_3 . The coordinates of the high symmetry "K" point for particular cell is listed in the last column. In the case of monolayer $c \rightarrow \infty$, then $p \rightarrow 0$.

supercell	\vec{a}_1	\vec{a}_2	\vec{a}_3	\vec{b}_1	\vec{b}_2	\vec{b}_3	K in RLV
ML "p"	(a/2 - $\sqrt{3}a/2$ 0)	(a/2 $\sqrt{3}a/2$ 0)	(0 0 c)	(k -m 0)	(k m 0)	(0 0 p)	(1/3 1/3 0)
ML "e"	(a 0 0)	(0 $\sqrt{3}a$ 0)	(0 0 c)	(k 0 0)	(0 m 0)	(0 0 p)	(1/3 0 0)
Bulk "p"	(a/2 $\sqrt{3}a/2$ 0)	(-a/2 - $\sqrt{3}a/2$ 0)	(-x 0 $\sqrt{c^2 - x^2}$)	(k m t)	(-k m -t)	(0 0 p1)	(- $\frac{1}{3}$ $\frac{1}{3}$ $\frac{2t}{3p1}$)
Bulk "e"	(a 0 0)	(0 $\sqrt{3}a$ 0)	(-x 0 $\sqrt{c^2 - x^2}$)	(k 0 t)	(0 m 0)	(0 0 p1)	(-1/3 0 t/(3p1))

are taken to sample the first Brillouin zone (BZ) on Γ -centered symmetry reduced Monkhorst-Pack meshes using a Gaussian smearing with $\sigma=0.05$ eV. However, in the case of the density of states (DOS) and frequency dependent function $\varepsilon(\omega)$ the tetrahedron method was employed along with the denser k-point grids for laterally rectangular supercell $20 \times 12 \times 1$ (ML "e" supercell) and $20 \times 12 \times 18$ (bulk "e" supercell), which was checked to be sufficient in convergence tests.

It is well known that standard exchange correlation functionals such as LDA and GGA are insufficient to describe a non-local nature of dispersive forces, which are crucial in proper description of many systems such as layered materials [65, 66] and adsorption molecules on the surfaces [67–70]. Here, we adopted a semi-empirical Grimme method [71] with a D3 parametrization (DFT-D3) [72]. Note that the Grimme approach is a commonly used technique for many vdW layered materials such as TMDs [73] MPX3 [26]. In particular, The DFT-D approach reproduce a good interlayer spacings in bulk graphite and other 2D layered systems [74, 75]. In order to model the monolayer, a 25 Å of vacuum is added to avoid spurious interactions between replicates. The lattice parameters are fully optimized for given magnetic state. All of the atoms are relaxed until the maximal force per atom was less than 10^{-3} eV/Å, and the maximal component of stress tensor is less than 0.3 kbarr for monolayers and 0.05 kbarr for bulk structures. A collinear arrangement of spins are assumed without inclusion of spin-orbit interaction.

DFT+U formalism proposed by Dudarev [76] is employed to properly characterize on-site Coulomb repulsion between 3d electrons of Mn ions, by using effective Hubbard U ($U_{eff} = U - J$, where $J=1$ eV). For each of the U, we have fully optimized lattice parameters.

Effective masses

In order to account for the anisotropic properties of the studied systems, we calculate the effective mass (m^*) tensor defined as:

$$\left(\frac{1}{m^*} \right)_{ij} = \frac{1}{\hbar^2} \frac{\partial^2 E_n(\vec{k})}{\partial k_i \partial k_j}, \quad i, j = x, y, z \quad (\text{S1})$$

where $E_n(\vec{k})$ is a dispersion relation for the n-th electronic band. The second derivatives are computed numerically using finite difference method, on a five-point stencil grid as implemented in the code [77]. Then, the effective mass tensor is diagonalized, and hence its components: m_1^*, m_2^*, m_3^* are determined along three principle axes in reciprocal space.

Dielectric screening

The static dielectric constant is a sum of two contributions $\varepsilon_0 = \varepsilon_\infty + \varepsilon^p$, where ε_∞ is electronic contribution (dielectric constant at optical frequency), where ε^p is ionic response to static electric fields (phononic part). The electronic term is calculated using density functional perturbation theory in the Independent Particle (IP) approach neglecting the local field effects ε_{IP}^{LR} [29], on the top of the PBE+U level. The ionic part is computed in the finite difference approach. The electronic and phononic contributions are presented in Table S2 and Table S3, respectively. Note, that both contributions are of the same order, indicating that the MnPS₃ is partially ionic system.

TABLE S2. Static dielectric constants ε_{ij} (electronic contribution) and 2D polarizability χ^{\parallel} calculated for the monolayer and bulk systems. The static dielectric properties are calculated by means of density functional perturbation theory in the independent particle approach (IP) neglecting local field effects.

Magn.	U [eV]	χ_{ML}^{\parallel} [Å]	χ_{BULK}^{\parallel} [Å]	BULK $\varepsilon_{xx} = \varepsilon_{yy}, \varepsilon_{zz}$
AFM-N	3	3.45	3.50	7.75 5.88
	5	3.25	3.29	7.33 5.67
AFM-z	3	3.49	3.49	7.72 5.84
	5	3.25	3.44	7.60 5.82
AFM-s	3	3.42	3.46	7.68 5.86
	5	3.24	3.42	7.56 5.83
FM	3	3.38	3.42	7.59 5.79
	5	3.32	3.26	7.27 5.64

TABLE S3. Ionic contribution ε^p to static dielectric constant obtained by means of finite-difference approach for bulk systems.

Magn.	U [eV]	ε_{xx}^p	ε_{yy}^p	ε_{zz}^p
AFM-N	3	4.93	4.84	0.46
	5	4.60	4.52	0.46
AFM-z	3	5.03	4.69	0.45
	5	4.64	4.44	0.46
AFM-s	3	5.04	5.16	0.46
	5	4.66	4.67	0.46
FM	3	5.14	5.05	0.45
	5	4.64	4.44	0.46

The 2D polarizability χ_{\parallel} is calculated as it was recently proposed in Ref. [35] as $\varepsilon(L_c) = 1 + \frac{4\pi\chi_{\parallel}}{L_c}$, where we neglect the higher order terms and ε is the in-plane dielectric constant, whereas L_c is the interlayer separation between the centers of adjacent layers (in the case of monolayer $L_c=c$, where c is lattice constant, in the case of bulk L_c is a vertical distance between the centers of adjacent layers). Note, that 2D polarizability calculated for ML and bulk give similar results (see Table S2), justifying this approach.

Selection rules

The direct interband momentum (optical) matrix elements between the VBM and CBM at \mathbf{k} point ($\mathbf{p}_{cv\mathbf{k}}$) are computed from the wave function derivatives using density functional perturbation theory [29]. The dipole selection rules are $|\mathbf{x} \cdot \mathbf{p}_{cv\mathbf{k}}|^2 > 0 \leftrightarrow x$, $|\mathbf{y} \cdot \mathbf{p}_{cv\mathbf{k}}|^2 > 0 \leftrightarrow y$, $|\mathbf{z} \cdot \mathbf{p}_{cv\mathbf{k}}|^2 > 0 \leftrightarrow z$, with the linear polarization given by $\mathbf{x} = (1, 0, 0)$, $\mathbf{y} = (0, 1, 0)$ and $\mathbf{z} = (0, 0, 1)$ (for more details see [62]).

B. Exciton calculations

The excitonic binding energies (shown in Fig. 2 of the main text) are obtained via the effective Bethe-Salpeter equation (BSE)[38, 43, 58]. Considering excitons arising from one conduction and one valence band with (anisotropic) parabolic dispersion, the BSE can be written as

$$[\Delta_{cv}(\vec{k}) - \Omega_N] A_N(\vec{k}) - \sum_{\vec{k}'} V(\vec{k}, \vec{k}') A_N(\vec{k}') = 0, \quad (S2)$$

in which $\Delta_{cv}(\vec{k}) = E_c(\vec{k}) - E_v(\vec{k})$, $E_c(\vec{k})$ and $E_v(\vec{k})$ are the conduction and valence bands that constitutes the exciton (in principle, from different points of the Brillouin zone), Ω_N and $A_N(\vec{k})$ are the energy and the envelope function of the N -th exciton state, respectively,

and the electron-hole interaction is given by the potential $V(\vec{k}, \vec{k}')$. Although the BSE given in Eq. (S2) is general and applies to the monolayer and bulk cases, the energy bands and electron-hole interaction potential are different for each case. For example, in monolayers the wavevector \vec{k} is a two-dimensional vector restricted to the plane and $E_c(\vec{k})$, $E_v(\vec{k})$ and $V(\vec{k}, \vec{k}')$ (the Rytova-Keldysh potential[59, 60]) take the specific form

$$\begin{aligned} E_c(\vec{k}) &= E_c + \frac{\hbar^2}{2m_e} \left(\frac{k_x^2}{m_{c,x}^*} + \frac{k_y^2}{m_{c,y}^*} \right), \\ E_v(\vec{k}) &= \frac{\hbar^2}{2m_e} \left(\frac{k_x^2}{m_{v,x}^*} + \frac{k_y^2}{m_{v,y}^*} \right), \\ V(\vec{k}, \vec{k}') &= \frac{1}{\mathcal{A}} \frac{e^2}{2\varepsilon_0} \frac{1}{\varepsilon \left| \vec{k} - \vec{k}' \right| + r_0 \left| \vec{k} - \vec{k}' \right|^2}, \end{aligned} \quad (S3)$$

in which \hbar is the Planck's constant, m_0 is the free electron mass, E_c is the band edge of the conduction band, $m_{c(v),x(y)}^*$ is the effective mass of conduction (valence) band along the k_x (k_y) directions, \mathcal{A} is the unit area, e is the electron charge, ε_0 is the vacuum permittivity, r_0 is the screening length of the 2D material ($r_0 = 2\pi\chi_{ML}^{\parallel}$), and ε is the effective dielectric constant that takes into account the dielectric screening of the surroundings ($\varepsilon = 1$ is a monolayer in vacuum). For the bulk case, the wavevector \vec{k} is a three-dimensional vector and $E_c(\vec{k})$, $E_v(\vec{k})$ and $V(\vec{k}, \vec{k}')$ (the anisotropic Coulomb potential[61]) are then given by

$$\begin{aligned} E_c(\vec{k}) &= E_c + \frac{\hbar^2}{2m_0} \left(\frac{k_x^2}{m_{c,x}^*} + \frac{k_y^2}{m_{c,y}^*} + \frac{k_z^2}{m_{c,z}^*} \right), \\ E_v(\vec{k}) &= \frac{\hbar^2}{2m_0} \left(\frac{k_x^2}{m_{v,x}^*} + \frac{k_y^2}{m_{v,y}^*} + \frac{k_z^2}{m_{v,z}^*} \right), \\ V(\vec{k}, \vec{k}') &= \frac{1}{\mathcal{V}} \frac{e^2}{\varepsilon_0} \left[\sum_a^{\{x,y,z\}} \varepsilon_{aa} (k_a - k'_a)^2 \right]^{-1}, \end{aligned} \quad (S4)$$

in which \mathcal{V} is the unit volume, ε_{aa} is the static dielectric constant along the a direction ($a = \{x, y, z\}$, and particularly, $\varepsilon_{xx} = \varepsilon_{yy} \neq \varepsilon_{zz}$).

We solved the BSE numerically considering a k -grid of $-k_L$ to k_L in every dimension sampled with $(2N_k + 1)^n$ with $n = 2$ for monolayers and $n = 3$ for bulk. The final values of the exciton binding energies are then obtained using a linear extrapolation of the values calculated in the k -grid sampled with different number of points. For instance, in the monolayer case we used $k_L = 0.6 \text{ \AA}^{-1}$ and $N_k = \{60, 61\}$. In the bulk case, we used $k_L = 0.5 \text{ \AA}^{-1}$ and $N_k = \{19, 20\}$. All the numerical inputs for the BSE, i.e., effective masses and dielectric constants are extracted from the first-principles calculations performed

here. Particularly, the values for the effective masses in the monolayer case are taken from Table II A. The effective masses for the bulk case are taken from Table II A and rotated to the k_x , k_y and k_z using the angles, also given in the table. The values for the 2D polarizability of the monolayers, χ_{ML}^{\parallel} , and the bulk static dielectric constants are given in Table S2.

II. RESULTS

A. DFT studies.

The choice of the U parameter. The standard exchange-correlation functionals such LDA, GGA are known to inadequately describe strongly correlated systems which contain transition metals (3d states), as well as are known to underestimate the bands gaps of semiconductors. In order to correctly describe the 3d states of Mn ions, we used DFT+U formalism proposed by Dudarev [76], where exchange coupling J is considered via an effective Hubbard U_{eff} coupling constant $U_{eff} = U - J$, denoted throughout the paper as U . The DFT+U method is essentially empirical, in the sense that U parameter must be provided. It is worth to mention that there is no standard procedure of obtaining U value for strongly correlated materials.

Firstly, we present how the band gaps depend on the Hubbard U parameter, for the magnetic groundstate (AFM-N) (see Fig. S1). Note, that the band gap increases as a function of U , approaching the maximal values of 2.9 eV, for nonphysically high value of $U=10$ eV. Note, that it is not possible to chose the parameter U , for which the band gap would approach the experimental value for the bulk 3.0 eV [20], or it would be equal to the band gap obtained from hybrid functional HSE06, which is equal to 3.26 eV for monolayer (similar value have been reported previously [27]). In the case of the exciton calculations employed in this study, the crucial issue is the dispersion of the bands near the Fermi level. Thus, we present the comparison between the electronic structure obtained for using hybrid functional HSE06 and two different values of Hubbard U , namely, $U=3$ eV and $U=5$ eV (see Fig. S2). Despite the fact, that the band gap in DFT+U approach is underestimated, however, the dispersion of the bands looks similar, especially for the case of $U=3$ eV, in comparison to HSE06 functional, similar results have been reported recently in [78]. Thus, the $U=3$ eV have been chosen for the further calculations, and also $U=5$ eV for the comparison purposes and to assess the impact of U parameter on physical properties.

Electronic properties. The summarized results of electronic properties for monolayers and bulk systems in respect to employed here magnetic states are collected in the Table S4 and Table S5, respectively. In order to determine the VBM and CBM of the bulk systems, we precisely probe the half of an entire first BZ zone, to

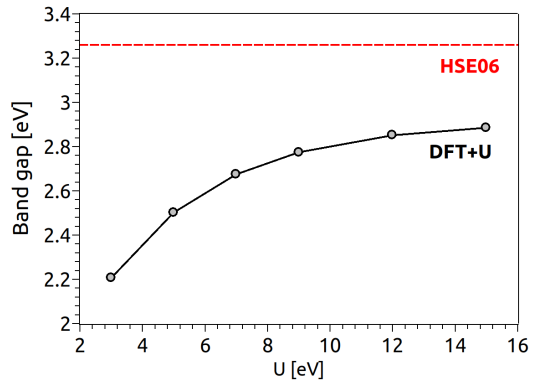


FIG. S1. Dependence of the band gap on the Hubbard U parameter obtained for the ground state of the monolayer. The dotted red line indicates the result obtained for the monolayer and using hybrid functional HSE06.

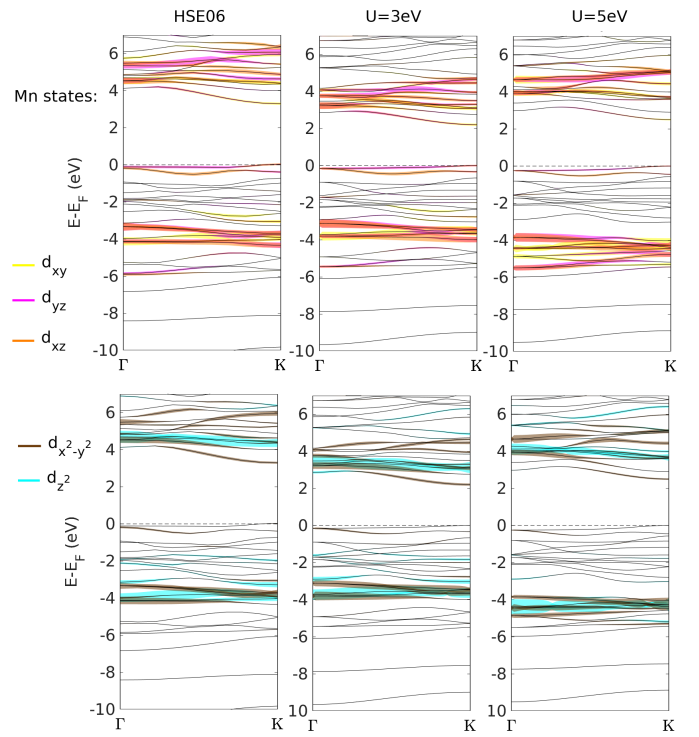


FIG. S2. Bands projections of the 3d Mn states for: (A) HSE06 hybrid functional, (B) Hubbard $U=3$ eV, and (C) $U=5$ eV for the magnetic ground state of ML.

directly show from which k -points the transition occurs. The exact coordinates of the valence band maximum and conduction band minimum are listed in Table S5. Our results reveal (see Table S5) that the bulk MnPS_3 is a wide semiconductor [20, 26, 79], and the predicted band gap for the groundstate (AFM-N) is consistent with previously reported values for the bulk [27]. Moreover, the band gaps depend on the magnetic state of the Mn ions (see Tables S4 and S5), namely, differ from few tens to

few hundredths of electronovolts from each other, independently of U parameter. The smallest band gap is obtained in case of AFM-s spin configuration. In addition, the band gaps of bulk are smaller than monolayer ones approximately hundredths of meV, which is consistent with band gap trend of the other layered materials. The similar dependence of Hubbard U on the band gaps are observed for the monolayer and bulk systems.

In the case of the effective mass calculations, it is worth to mention, that for the monolayer systems, the principle reciprocal axes coincide with the Cartesian reciprocal axes, and the m_1^* and m_2^* components can be considered as in-plane (001) components (within the layer) denoted here as m_1^{\parallel} and m_2^{\parallel} , respectively. Note, that m_3^* is out-of-plane (001) component (out of the layer) denoted as m_3^{\perp} and for all monolayer systems approaches infinity and thus, it is not presented. However, for the bulk case, only m_2^* can be considered as in-plane (001) component (m_2^{\parallel}), the other two m_1^* , m_3^* are rotated counterclockwise at the angle of Θ from [100] and [010] crystallographic directions in reciprocal space, respectively (rotation about

y-axis, Θ angles are listed in Table S5). In addition, the AFM-z and AFM-s magnetic configurations exhibit the anisotropic behaviour of in-plane effective masses. For AFM-s and AFM-z cases, the in-plane [100] direction can be considered as the mobile carrier direction (heavier carriers), than for [010] crystallographic direction, indicating the differences of the conductivity that could be measured within the monolayer plane. Note, that the in-plane components of effective masses can reveal the structural symmetry of MnPS_3 , namely the $m_1^{\parallel} = m_1^{\perp}$ can indicate the presence of hexagonal symmetry for FM, AFM-N cases, whereas the $m_1^{\parallel} \neq m_1^{\perp}$ breaking of this symmetry observed in AFM-s, AFM-z cases.

B. Exciton binding energies

Here we provide the exciton binding energies for bulk (Table S6) and monolayer (Table S7) of MnPS_3 . Although, we provide the exciton binding energy as a positive value, it lies below the single-particle band gap.

[1] B. Huang, G. Clark, E. Navarro-Moratalla, D. R. Klein, R. Cheng, K. L. Seyler, D. Zhong, E. Schmidgall, M. A. McGuire, D. H. Cobden, W. Yao, D. Xiao, P. Jarillo-Herrero, and X. Xu, Layer-dependent ferromagnetism in a van der Waals crystal down to the monolayer limit, *Nature* **546**, 270 (2017).

[2] C. Gong, L. Li, Z. Li, H. Ji, A. Stern, Y. Xia, T. Cao, W. Bao, C. Wang, Y. Wang, Z. Q. Qiu, R. J. Cava, S. G. Louie, J. Xia, and X. Zhang, Discovery of intrinsic ferromagnetism in two-dimensional van der Waals crystals, *Nature* **546**, 265 (2017).

[3] H. Li, S. Ruan, and Y.-J. Zeng, Intrinsic van der Waals magnetic materials from bulk to the 2d limit: New frontiers of spintronics, *Advanced Materials* **31**, 1900065 (2019).

[4] M. Gibertini, M. Koperski, A. F. Morpurgo, and K. S. Novoselov, Magnetic 2D materials and heterostructures, *Nature Nanotechnology* **14**, 408 (2019).

[5] C. Gong and X. Zhang, Two-dimensional magnetic crystals and emergent heterostructure devices, *Science* **363**, 10.1126/science.aav4450 (2019).

[6] W. Chen, Z. Sun, Z. Wang, L. Gu, X. Xu, S. Wu, and C. Gao, Direct observation of van der Waals stacking-dependent interlayer magnetism, *Science* **366**, 983 (2019).

[7] J. Kunstmann, F. Mooshammer, P. Nagler, Rodolfo, A. Chaves, F. Stein, N. Paradiso, G. Plechinger, C. Strunk, C. Schüller, G. Seifert, D. R. Reichman, and T. Korn, Momentum-space indirect interlayer excitons in transition-metal dichalcogenide van der Waals heterostructures, *Nature Physics* **14**, 10.1038/s41567-018-0123-y (2018).

[8] M. Birowska, J. Urban, M. Baranowski, D. K. Maude, P. Plochocka, and N. G. Szwacki, The impact of hexagonal boron nitride encapsulation on the structural and vibrational properties of few layer black phosphorus, *Nanotechnology* **30**, 195201 (2019).

[9] I. Žutić, A. Matos-Abiague, B. Scharf, H. Dery, and K. Belashchenko, Proximity-induced materials, *Materials Today* **22**, 85 (2019).

[10] K. Zollner, P. E. Faria Junior, and J. Fabian, Proximity exchange effects in MoSe_2 and WSe_2 heterostructures with CrI_3 : Twist angle, layer, and gate dependence, *Phys. Rev. B* **100**, 085128 (2019).

[11] A. Szuplewska, A. Rozmysłowska-Wojciechowska, S. Poźniak, T. Wojciechowski, M. Birowska, M. Popielski, M. Chudy, W. Ziemkowska, L. Chlubny, D. Moszczyńska, A. Olszyna, J. A. Majewski, and A. M. Jastrzebska, Multilayered stable 2D nano-sheets of Ti_2NT_x MXene: synthesis, characterization, and anticancer activity, *Journal of Nanobiotechnology* **17**, 114 (2019).

[12] G. L. Flem, R. Brec, G. Ouvard, A. Louisy, and P. Segransan, Magnetic interactions in the layer compounds MPX_3 ($\text{M} = \text{Mn, Fe, Ni}; \text{X} = \text{S, Se}$), *Journal of Physics and Chemistry of Solids* **43**, 455 (1982).

[13] R. Brec, Review on structural and chemical properties of transition metal phosphorous trisulfides MPS_3 , *Solid State Ionics* **22**, 3 (1986).

[14] F. Wang, T. A. Shifa, P. Yu, P. He, Y. Liu, F. Wang, Z. Wang, X. Zhan, X. Lou, F. Xia, and J. He, New frontiers on van der Waals layered metal phosphorous trichalcogenides, *Advanced Functional Materials* **28**, 1802151 (2018).

[15] P. A. Joy and S. Vasudevan, Magnetism in the layered transition-metal thiophosphates MPS_3 ($\text{M} = \text{Mn, Fe, and Ni}$), *Phys. Rev. B* **46**, 5425 (1992).

[16] K. Kurosawa, S. Saito, and Y. Yamaguchi, Neutron diffraction study on MnPS_3 and FePS_3 , *Journal of the Physical Society of Japan* **52**, 3919 (1983).

[17] S. Kang, K. Kim, B. H. Kim, J. Kim, K. I. Sim, J.-U. Lee, S. Lee, K. Park, S. Yun, T. Kim, *et al.*, Coherent many-body exciton in van der Waals antiferromagnet NiPS_3 ,

Nature **583**, 785 (2020).

[18] G. Long, T. Zhang, X. Cai, J. Hu, C.-w. Cho, S. Xu, J. Shen, Z. Wu, T. Han, J. Lin, *et al.*, Isolation and characterization of few-layer manganese thiophosphite, ACS nano **11**, 11330 (2017).

[19] R. N. Jenjeti, R. Kumar, M. P. Austeria, and S. Sampath, Field Effect Transistor Based on Layered NiPS₃, Scientific Reports **8**, 8586 (2018).

[20] K.-z. Du, X.-z. Wang, Y. Liu, P. Hu, M. I. B. Utama, C. K. Gan, Q. Xiong, and C. Kloc, Weak van der waals stacking, wide-range band gap, and raman study on ultrathin layers of metal phosphorus trichalcogenides, ACS Nano **10**, 1738 (2016).

[21] J. Chu, F. Wang, L. Yin, L. Lei, C. Yan, F. Wang, Y. Wen, Z. Wang, C. Jiang, L. Feng, J. Xiong, Y. Li, and J. He, High-Performance Ultraviolet Photodetector Based on a Few-Layered 2D NiPS₃ Nanosheet, Advanced Functional Materials **27**, 1701342 (2017).

[22] S. Lee, K.-Y. Choi, S. Lee, B. H. Park, and J.-G. Park, Tunneling transport of mono-and few-layers magnetic van der waals mnps3, APL Materials **4**, 086108 (2016).

[23] S. N. Neal, H.-S. Kim, K. A. Smith, A. V. Haglund, D. G. Mandrus, H. A. Bechtel, G. L. Carr, K. Haule, D. Vanderbilt, and J. L. Musfeldt, Near-field infrared spectroscopy of monolayer MnPS₃, Phys. Rev. B **100**, 075428 (2019).

[24] K. Kim, S. Y. Lim, J. Kim, J.-U. Lee, S. Lee, P. Kim, K. Park, S. Son, C.-H. Park, J.-G. Park, *et al.*, Antiferromagnetic ordering in van der Waals 2D magnetic material MnPS₃ probed by Raman spectroscopy, 2D Materials **6**, 041001 (2019).

[25] N. Sivadas, M. W. Daniels, R. H. Swendsen, S. Okamoto, and D. Xiao, Magnetic ground state of semiconducting transition-metal trichalcogenide monolayers, Phys. Rev. B **91**, 235425 (2015).

[26] B. L. Chittari, Y. Park, D. Lee, M. Han, A. H. MacDonald, E. Hwang, and J. Jung, Electronic and magnetic properties of single-layer MPX₃ metal phosphorous trichalcogenides, Phys. Rev. B **94**, 184428 (2016).

[27] J. Yangab, Y. Zhoua, Q. Guoa, D. Y., and E. Voloshina, Electronic, magnetic and optical properties of MnPX₃ (X = S, Se) monolayers with and without chalcogen defects: a first-principles study, RSC Adv. **10**, 851 (2020).

[28] B. Himmetoglu, A. Floris, S. de Gironcoli, and M. Cococcioni, Hubbard-corrected DFT energy functionals: The LDA+U description of correlated systems, International Journal of Quantum Chemistry **114**, 14 (2014).

[29] M. Gajdoš, K. Hummer, G. Kresse, J. Furthmüller, and F. Bechstedt, Linear optical properties in the projector-augmented wave methodology, Phys. Rev. B **73**, 045112 (2006).

[30] B.-C. Shih, Y. Xue, P. Zhang, M. L. Cohen, and S. G. Louie, Quasiparticle band gap of ZnO: High Accuracy from the Conventional G^0W^0 approach, Phys. Rev. Lett. **105**, 146401 (2010).

[31] H. Cao, Z. Yu, P. Lu, and L.-W. Wang, Fully converged plane-wave-based self-consistent gw calculations of periodic solids, Phys. Rev. B **95**, 035139 (2017).

[32] M. Shishkin, M. Marsman, and G. Kresse, Accurate quasiparticle spectra from self-consistent gw calculations with vertex corrections, Phys. Rev. Lett. **99**, 246403 (2007).

[33] M. Grumet, P. Liu, M. Kaltak, J. c. v. Klimeš, and G. Kresse, Beyond the quasiparticle approximation: Fully self-consistent gw calculations, Phys. Rev. B **98**, 155143 (2018).

[34] A. Molina-Sánchez and L. Wirtz, Phonons in single-layer and few-layer MoS₂ and WS₂, Phys. Rev. B **84**, 155413 (2011).

[35] T. C. Berkelbach, M. S. Hybertsen, and D. R. Reichman, Theory of neutral and charged excitons in monolayer transition metal dichalcogenides, Phys. Rev. B **88**, 045318 (2013).

[36] M. Bokdam, T. Sander, A. Stroppa, S. Picozzi, D. D. Sarma, C. Franchini, and G. Kresse, Role of polar phonons in the photo excited state of metal halide perovskites, Scientific Reports **6**, 28618 (2016).

[37] S. Albrecht, L. Reining, R. Del Sole, and G. Onida, Ab initio calculation of excitonic effects in the optical spectra of semiconductors, Phys. Rev. Lett. **80**, 4510 (1998).

[38] M. Rohlffing and S. G. Louie, Electron-hole excitations and optical spectra from first principles, Phys. Rev. B **62**, 4927 (2000).

[39] T. C. Berkelbach, M. S. Hybertsen, and D. R. Reichman, Theory of neutral and charged excitons in monolayer transition metal dichalcogenides, Phys. Rev. B **88**, 045318 (2013).

[40] A. Chernikov, T. C. Berkelbach, H. M. Hill, A. Rigosi, Y. Li, O. B. Aslan, D. R. Reichman, M. S. Hybertsen, and T. F. Heinz, Exciton Binding Energy and Nonhydrogenic Rydberg Series in Monolayer WS₂, Phys. Rev. Lett. **113**, 076802 (2014).

[41] Y. Cho and T. C. Berkelbach, Environmentally sensitive theory of electronic and optical transitions in atomically thin semiconductors, Phys. Rev. B **97**, 041409(R) (2018).

[42] K.-Q. Lin, C. Shen Ong, S. Bange, P. E. Faria Junior, B. Peng, J. D. Ziegler, J. Zipfel, C. Bäuml, N. Paradiso, K. Watanabe, *et al.*, Bright excitons with negative-mass electrons, arXiv , arXiv (2020).

[43] P. E. Faria Junior, M. Kurpas, M. Gmitra, and J. Fabian, $k \cdot p$ theory for phosphorene: Effective g -factors, landau levels, and excitons, Phys. Rev. B **100**, 115203 (2019).

[44] J. C. G. Henriques and N. M. R. Peres, Excitons in phosphorene: A semi-analytical perturbative approach, Phys. Rev. B **101**, 035406 (2020).

[45] B. Scharf, G. Xu, A. Matos-Abiague, and I. Žutić, Magnetic proximity effects in transition-metal dichalcogenides: Converting excitons, Phys. Rev. Lett. **119**, 127403 (2017).

[46] K. Zollner, P. E. Faria Junior, and J. Fabian, Giant proximity exchange and valley splitting in transition metal dichalcogenide/BN/(Co, Ni) heterostructures, Phys. Rev. B **101**, 085112 (2020).

[47] J. C. G. Henriques, G. Catarina, A. T. Costa, J. Fernández-Rossier, and N. M. R. Peres, Excitonic magneto-optical kerr effect in two-dimensional transition metal dichalcogenides induced by spin proximity, Phys. Rev. B **101**, 045408 (2020).

[48] D. Zhong, K. L. Seyler, X. Linpeng, N. P. Wilson, T. Taniguchi, K. Watanabe, M. A. McGuire, K.-M. C. Fu, D. Xiao, W. Yao, *et al.*, Layer-resolved magnetic proximity effect in van der Waals heterostructures, Nature Nanotechnology **15**, 187 (2020).

[49] D. Zhong, K. L. Seyler, X. Linpeng, R. Cheng, N. Sivadas, B. Huang, E. Schmidgall, T. Taniguchi, K. Watanabe, M. A. McGuire, *et al.*, Van der waals engineering of ferromagnetic semiconductor heterostructures for spin and valleytronics, Science advances **3**, e1603113 (2017).

[50] L. Ciorciaro, M. Kröner, K. Watanabe, T. Taniguchi, and A. Imamoglu, Observation of Magnetic Proximity Effect Using Resonant Optical Spectroscopy of an Electrically Tunable $\text{MoSe}_2/\text{CrBr}_3$ Heterostructure, *Phys. Rev. Lett.* **124**, 197401 (2020).

[51] A. V. Stier, N. P. Wilson, K. A. Velizhanin, J. Kono, X. Xu, and S. A. Crooker, Magneto-optics of exciton rydberg states in a monolayer semiconductor, *Phys. Rev. Lett.* **120**, 057405 (2018).

[52] A. Amo, M. D. Martín, L. Viña, A. I. Toropov, and K. S. Zhuravlev, Interplay of exciton and electron-hole plasma recombination on the photoluminescence dynamics in bulk GaAs, *Phys. Rev. B* **73**, 035205 (2006).

[53] A. V. Rodina, M. Dietrich, A. Göldner, L. Eckey, A. Hoffmann, A. L. Efros, M. Rosen, and B. K. Meyer, Free excitons in wurtzite GaN, *Phys. Rev. B* **64**, 115204 (2001).

[54] A. Beal, J. Knights, and W. Liang, Transmission spectra of some transition metal dichalcogenides. ii. group via: trigonal prismatic coordination, *Journal of Physics C: Solid State Physics* **5**, 3540 (1972).

[55] T. Goto, Y. Kato, K. Uchida, and N. Miura, Exciton absorption spectra of MoS_2 crystals in high magnetic fields up to 150 T, *Journal of Physics: Condensed Matter* **12**, 6719 (2000).

[56] N. Saigal, V. Sugunakar, and S. Ghosh, Exciton binding energy in bulk MoS_2 : A reassessment, *Applied Physics Letters* **108**, 132105 (2016).

[57] A. Arora, M. Koperski, K. Nogajewski, J. Marcus, C. Faugeras, and M. Potemski, Excitonic resonances in thin films of WSe_2 : from monolayer to bulk material, *Nanoscale* **7**, 10421 (2015).

[58] D. Tedeschi, M. De Luca, P. E. Faria Junior, A. Grana-dos del Águila, Q. Gao, H. H. Tan, B. Scharf, P. C. M. Christianen, C. Jagadish, J. Fabian, and A. Polimeni, Unusual spin properties of InP wurtzite nanowires revealed by Zeeman splitting spectroscopy, *Phys. Rev. B* **99**, 161204(R) (2019).

[59] N. S. Rytova, The screened potential of a point charge in a thin film, *Mosc. Univ. Phys. Bull.* **3**, 18 (1967).

[60] L. Keldysh, Coulomb interaction in thin semiconductor and semimetal films, *Sov. J. Exp. Theo. Phys. Lett.* **29**, 658 (1979).

[61] L. D. Landau, J. Bell, M. Kearsley, L. Pitaevskii, E. Lifshitz, and J. Sykes, *Electrodynamics of continuous media*, Vol. 8 (Elsevier, 2013).

[62] T. Wozniak, P. E. Faria Junior, G. Seifert, A. Chaves, and J. Kunstmann, Exciton g factors of van der Waals heterostructures from first-principles calculations, *Phys. Rev. B* **101**, 235408 (2020).

[63] G. Kresse and J. Hafner, Ab initio, *Phys. Rev. B* **47**, 558 (1993).

[64] G. Kresse and J. F. Müller, Efficiency of ab-initio total energy calculations for metals and semiconductors using a plane-wave basis set, *Computational Materials Science* **6**, 15 (1996).

[65] S. A. Tawfik, T. Gould, C. Stampfl, and M. J. Ford, Evaluation of van der Waals density functionals for layered materials, *Phys. Rev. Materials* **2**, 034005 (2018).

[66] M. Birowska, K. Milowska, and J. A. Majewski, Van Der Waals Density Functionals for Graphene Layers and Graphite, *Acta Physica Polonica A* **120**, 845 (2011).

[67] J. Tao and A. M. Rappe, Physical adsorption: Theory of van der Waals interactions between particles and clean surfaces, *Phys. Rev. Lett.* **112**, 106101 (2014).

[68] M. Birowska, M. E. Marchwiany, C. Draxl, and J. A. Majewski, Assessment of approaches for dispersive forces employing semihydrogenated graphene as a case study, *Computational Materials Science* **186**, 109940 (2021).

[69] K. Milowska, M. Birowska, and J. A. Majewski, Ab initio study of functionalized carbon nanotubes, *Acta Physica Polonica A* **116**, 841 (2009).

[70] K. Milowska, M. Birowska, and J. A. Majewski, Mechanical, electrical, and magnetic properties of functionalized carbon nanotubes, *AIP Conference Proceedings* **1399**, 827 (2011).

[71] S. Grimme, Semiempirical GGA-type density functional constructed with a long-range dispersion correction, *J. Comput. Chem.* **27**, 1787 (2006).

[72] S. Grimme, J. Antony, S. Ehrlich, and H. Krieg, A consistent and accurate ab initio parametrization of density functional dispersion correction (DFT-D) for the 94 elements H-Pu, *J. Chem. Phys.* **132**, 154104 (2010).

[73] S. K. Pandey, R. Das, and P. Mahadevan, Layer-dependent electronic structure changes in transition metal dichalcogenides: The microscopic origin, *ACS Omega* **5**, 15169 (2020).

[74] W. Reckien, F. Janetzko, M. F. Peintinger, and T. Bredow, Implementation of empirical dispersion corrections to density functional theory for periodic systems, *Journal of Computational Chemistry* **33**, 2023 (2012), <https://onlinelibrary.wiley.com/doi/pdf/10.1002/jcc.23037>.

[75] T. Björkman, A. Gulans, A. V. Krasheninnikov, and R. M. Nieminen, Are we van der Waals ready?, *Journal of Physics: Condensed Matter* **24**, 424218 (2012).

[76] S. L. Dudarev, G. A. Botton, S. Y. Savrasov, C. J. Humphreys, and A. P. Sutton, Electron-energy-loss spectra and the structural stability of nickel oxide: An LSDA+U study, *Phys. Rev. B* **57**, 1505 (1998).

[77] A. Fonari and C. Sutton, Effective mass calculator, "<https://github.com/afonari/emc>" (2012).

[78] J. Yang, Y. Zhou, Q. Guo, Y. Dedkov, and E. Voloshina, Electronic, magnetic and optical properties of MnPX_3 ($X = \text{S}, \text{Se}$) monolayers with and without chalcogen defects: a first-principles study, *RSC Advances* **10**, 851 (2020).

[79] R. Brec, D. M. Schleich, G. Ouvrard, A. Louisy, and J. Rouxel, Physical properties of lithium intercalation compounds of the layered transition-metal chalcogenophosphites, *Inorganic Chemistry* **18**, 1814 (1979).

TABLE S4. Calculated band gaps, valence and conduction edges, and effective masses of monolayer for various magnetic states of Mn ions. The symbol D, sD, ID in parenthesis indicate the direct band gap, semi direct band gap, indirect band gap, respectively. Note that the sD band gap occurs in very close vicinity of high symmetry K point in BZ, and in good approximation can be further considered as direct. The m_1^{\parallel} and m_2^{\parallel} are determined along (1 0 0) and (0 1 0) directions in Cartesian reciprocal space, respectively and are given in m_e unit.

magn.	U [eV]	band gap [eV]	VBM	CBM	$m_1^{\parallel}, m_2^{\parallel}$ - hole [m_e]	$m_1^{\parallel}, m_2^{\parallel}$ - electron [m_e]
AFM-N	3	2.206 (D)	K	K	-1.26, -1.25	0.68, 0.68
	5	2.502 (D)	K	K	-0.96, -0.95	0.58, 0.58
AFM-z	3	1.969 (sD)	near K	near K	-1.34, -0.90	0.61 0.90
	5	2.345 (sD)	near K	near K	-1.03, -0.85	0.55, 0.71
AFM-s	3	1.795 (D)	K	K	-0.79, -0.77	0.77, 0.53
	5	2.207 (D)	K	K	-0.78, -0.73	0.62, 0.51
FM (\uparrow)	3	2.268 (D)	K	K	-0.60, -0.60	0.40, 0.40
	5	2.412 (ID)	K	Γ	-0.60, -0.60	0.30, 0.30

TABLE S5. Calculated band gaps for various magnetic states of Mn atoms for the bulk. The fractional coordinates of the valence band maximum (VBM) and conduction band minimum (CBM) given in reciprocal lattice vectors (RLV) are collected in the columns 5 and 6, respectively. Note, that the coordinates of the high symmetry K point folded to the "e" supercell (sc) for AFM-z and AFM-s is $(-1/3 \ 0 \ 0.110)$ in RLV, whereas in the case of "p" supercell for FM and AFM-N states is $(1/3, -1/3, 0.22)$ in RLV, which have been calculated accordingly with the values given in Table S1. The direction of the principal axes m_1^* and m_3^* are counterclockwise rotated at the angle Θ from [100] and [001] directions, respectively.

magn. state	U [eV]	band gap [eV]	k-point of VBM	k-point of CBM	sc	mass	hole [m_e]	electron [m_e]	electron [m_e]	
AFM-N	3	2.041 (ID) (2.106 D) $\Delta_{gap}^{ID-D} = 65$ meV	$(1/3 \ -1/3 \ 0.264)$	$(-1/3 \ 1/3 \ 0.426)$	p	m_1	-1.15	0.60	0.80	
						m_2^{\parallel}	-1.27	0.69	0.70	
						m_3	-2.25	5	-7.27	
						Θ	57.0	2.9	5.58	
	5	2.352 (ID) (2.369 D) $\Delta_{gap}^{ID-D} = 17$ meV	$(1/3 \ -1/3 \ 0.279)$	$(-1/3, \ 1/3, \ 0.44)$		m_1	-1.15	0.51	0.70	
						m_2^{\parallel}	-0.96	0.59	0.60	
						m_3	-2.11	4.17	-6.04	
						Θ	30.0	2.8	5.01	
AFM-z	3	1.828 (ID) (1.840 D) $\Delta_{gap}^{ID-D} = 12$ meV	$(-0.300 \ 0 \ 0.289)$	$(1/3 \ 0 \ 0.441)$	e	m_1	-1	0.56	0.62	
						m_2^{\parallel}	-0.86	0.98	0.99	
						m_3	-4.13	5.09	-31.16	
						Θ	30.9	2.7	5.85	
	5	2.212 (ID) (2.225 D) $\Delta_{gap}^{ID-D} = 13$ meV	$(-1/3 \ 0 \ 0.317)$	$(1/3 \ 0 \ 0.454)$		m_1	-0.86	0.49	0.59	
						m_2^{\parallel}	-0.91	0.74	0.73	
						m_3	-3.63	4.01	107.52	
						Θ	16.2	3.0	5.01	
AFM-s	3	1.653 (ID) (1.656 D) $\Delta_{gap}^{ID-D} = 3$ meV	$(0.367 \ 0 \ 0.427)$	$(1/3 \ 0 \ 0.482)$	e	m_1	-0.63	0.7	0.76	
						m_2^{\parallel}	-0.87	0.55	0.52	
						m_3	-1.97	5.29	5.67	
						Θ	2.6	6.5	4.44	
	5	2.066 (ID) (2.067 D) $\Delta_{gap}^{ID-D} = 1$ meV	$(0.367 \ 0 \ 0.441)$	$(1/3 \ 0 \ 0.482)$		m_1	-0.64	0.56	0.60	
						m_2^{\parallel}	-0.92	0.53	0.52	
						m_3	-2.17	4.12	4.35	
						Θ	4.4	4.9	3.63	
FM (\uparrow)	3	2.096	$(-1/3 \ 0 \ 0.414)$	$(1/3 \ 0 \ 0.414)$	e	m_1	-0.54	0.44	0.43	
						m_2^{\parallel}	-0.56	0.42	0.44	
						m_3	-4.05	-4.20	-1.88	
						Θ	5.3	0	3.14	
	5	2.276 (ID) (2.419 D) $\Delta_{gap}^{ID-D} = 143$ meV	$(-1/3 \ 0 \ 0.400)$	$(0 \ 0 \ 0)$	e	m_1	-0.54	0.26	0.43	
						m_2^{\parallel}	-0.57	0.27	0.45	
						m_3	-4.15	1.63	-1.94	
						Θ	5.2	4.3	3.4	

TABLE S6. Exciton binding energies for bulk MnPS₃.

	direct		indirect	
	U=3eV	U=5eV	U=3eV	U=5eV
AFM-N	177.09	185.21	150.83	151.31
AFM-s	137.15	135.87	136.15	133.97
AFM-z	177.33	170.77	159.94	150.26
FM			160.69	92.43

TABLE S7. Exciton binding energies for monolayer MnPS₃ considering different values of the effective dielectric constant of the surroundings.

ϵ	AFM-N		AFM-z		AFM-s		FM	
	U=3eV	U=5eV	U=3eV	U=5eV	U=3eV	U=5eV	U=3eV	U=5eV
1	1027.01	1017.06	1022.86	1025.83	971.85	987.48	881.07	843.90
2	672.11	651.27	668.75	658.32	623.32	625.72	545.45	512.12
3	493.07	469.35	490.12	475.83	450.17	447.55	383.02	354.16
4	382.86	359.18	380.00	364.55	344.89	339.84	286.87	262.22
5	307.39	285.29	304.96	290.02	273.68	268.17	223.63	202.21